

Treatment-aware Diffusion Probabilistic Model for Longitudinal MRI Generation and Diffuse Glioma Growth Prediction

Qinghui Liu, Elies Fuster-Garcia, Ivar Thokle Hovden, Donatas Sederevičius, Karoline Skogen, Bradley J MacIntosh, Edvard Grødem, Till Schellhorn, Petter Brandal, Atle Bjørnerud, and Kyrre Eeg Emblem

Abstract—Diffuse gliomas are malignant brain tumors that grow widespread through the brain. The complex interactions between neoplastic cells and normal tissue, as well as the treatment-induced changes often encountered, make glioma tumor growth modeling challenging. In this paper, we present a novel end-to-end network capable of generating future tumor masks and realistic MRIs of how the tumor will look at any future time points for different treatment plans. Our approach is based on cutting-edge diffusion probabilistic models and deep-segmentation neural networks. We included sequential multi-parametric magnetic resonance images (MRI) and treatment information as conditioning inputs to guide the generative diffusion process. This allows for tumor growth estimates at any given time point. We trained the model using real-world post-operative longitudinal MRI data with glioma tumor growth trajectories represented as tumor segmentation maps over time. The model has demonstrated promising performance across a range of tasks, including the generation of high-quality synthetic MRIs with tumor masks, time-series tumor segmentations, and uncertainty estimates. Combined with the treatment-aware generated MRIs, the tumor growth predictions with uncertainty estimates can provide useful information for clinical decision-making.

Index Terms—Diffuse glioma growth, Longitudinal MRI, Diffusion probabilistic model, Deep learning.

I. INTRODUCTION

DIFFUSE gliomas are the most common central nervous system tumors [1], accounting for 80% of all malignant

brain tumors, 30% of all primary brain tumors, and a major cause of death from primary brain tumors [2]. Despite advances in diagnosis and therapy, the prognosis of diffuse glioma patients, particularly those with glioblastomas, remains poor. Glioblastoma patients have a median survival time of less than 15 months after initial diagnosis [3], [4]. Only very few treatment improvements have been made the last 20 years, and new approaches are highly needed to better understand and estimate glioma tumor growth and treatment response. Improved growth prediction can provide useful insights for diagnosis, prognosis, personalized medicine, and therapy planning.

In the past, the tumor growth prediction problem has been approached through mathematical models from biological principles, such as ones based on the reaction-diffusion (RD) equation [5]–[7]. A few recent RD-based methods [8]–[10] have introduced different approaches to adjust the model’s parameters towards precise personalizing brain tumor modeling. However, the success of these approaches depends on the quality of the chosen forward model, which tends to include simplifying assumptions compared to the actual biological processes [11]. The simplified and insufficient parameters of RD-based methods might not be sufficient to model the inherent complexities of the growth patterns of the tumors [12].

Recently, deep-learning-based approaches have been developed to address the glioma growth prediction problem [11]–[13], by learning growth patterns directly from the MRI data. However, all of these approaches have been constrained to using only image data to predict tumor masks while ignoring the effects of any other factors, such as the administered treatment and changes in it. These interventions clearly influence glioma growth behavior and should be accounted for. Available deep-learning models also lack the ability to generate future MR images and associated uncertainty maps. Collectively, these limitations are barriers to clinical translation.

Other researchers argue that the growth process is not deterministic (e.g. in [11]) and it is important to account for tractable treatment (past, present, and future) and other patient-specific factors that contribute to glioma tumor growth characteristics. Figure 1 shows an example of longitudinal glioma progression in relation to specific therapy and days after surgery. Producing treatment-aware future MRI alongside possible tumor masks, as well as quantifying their evolution uncertainty, could lead to improved personalized treatment

This work was supported by the European Union’s Horizon 2020 Programme: ERC Grant Agreement No. 758657-ImPRESS, Helse Sør-Øst Regional Health Authority grants 2021057, 2017073, the Research Council of Norway grants 325971, 261984, and grant PID2021-127110OA-I00 (PROGRESS) funded by MCIN/AEI/10.13039/501100011033 from Agencia de Investigación de Espana and by ERDF A way of making Europe.

Q. Liu, I. T. Hovden, D. Sederevičius, K. Skogen, B. J. MacIntosh, E. Grødem, T. Schellhorn, P. Brandal, A. Bjørnerud and K. E. Emblem are with the Department of Physics and Computational Radiology, Oslo University Hospital (OUS), Rikshospitalet, 0372 Oslo, Norway (e-mail: qiliu@ous-hf.no; ivarth@student.matnat.uio.no; donseds@ous-hf.no; kaskog@ous-hf.no; brad.macintosh@utoronto.ca; edvard.grodem@gmail.com; UXSCTI@ous-hf.no; pebra@ous-hf.no; atle.bjornerud@fys.uio.no, kemblem@ous-hf.no).

E. Fuster-Garcia is with the Biomedical Data Science Laboratory, Instituto Universitario de Tecnologías de la Información y Comunicaciones, Universitat Politècnica de València, 46022 Valencia, Spain (e-mail: elies.fuster@gmail.com).

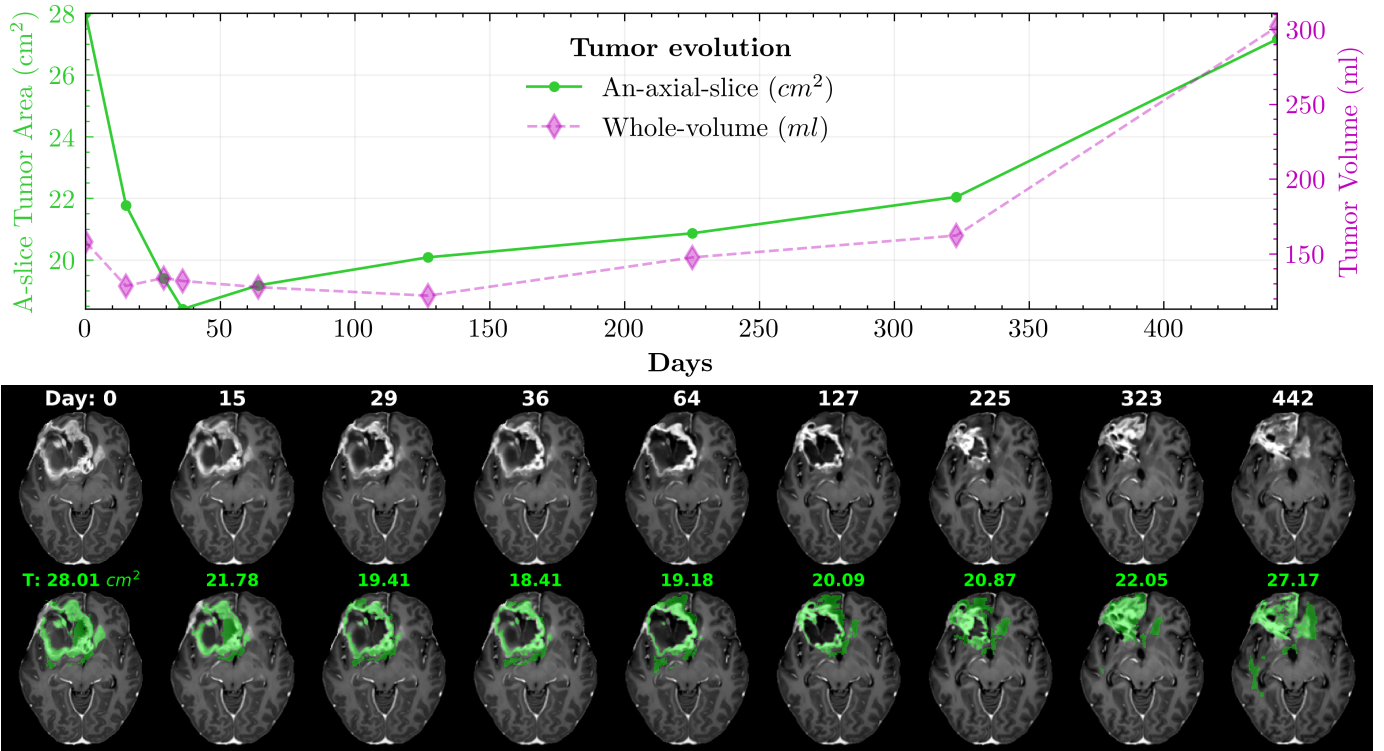


Fig. 1. An example of longitudinal glioma tumor (including both the edema and the contrast-enhancing tumor marked with green color) evolution based on post-operation treatments and days: from day 0 to 36 using chemoradiation (CRT) and from day 64 to day 442 with temozolomide (TMZ). Note that the first scan (Day 0) was taken four weeks after surgery/initial resection.

planning and, ultimately, better patient outcomes. To this end, we investigate a novel solution, by leveraging advances in denoising diffusion probabilistic models (DDPM) [14]–[16] with representation learning [17]–[19], and propose a versatile end-to-end generative model, so-called Treatment-aware Diffusion (TaDiff) probabilistic model. An overview of the TaDiff model is illustrated in Figure 2. Overall, we developed treatment-aware embedding and joint-task learning methods that enable the TaDiff model to learn tumor growth dynamics from source MRI sequences with treatment variables. The learned model can then predict tumor growth probabilities based on target treatment information and source treatment MRI sequences, construct future MRIs using a reverse diffusion process, and produce tumor evolution uncertainty based on multiple sampling.

II. RELATED WORK

One of the distinguishing features of diffuse glioma growth, particularly glioblastoma¹, is the highly irregular and unpredictable growth patterns involving multiple tissue types, which make the prediction of diffuse glioma growth notoriously difficult [21]. The majority of existing approaches that model diffuse glioma growth are based on variants of reaction-diffusion equation characterizing tumor invasion (diffusion term) and proliferation (reaction term) [22]–[24]. To capture mechanical deformation, the reaction-diffusion model can be

coupled to a linear elasticity model for brain and tumor mechanical properties [22], [25]. Extension of these models coupled to nonlinear elasticity has also been presented [26]–[28], but these models are more difficult to calibrate either because they are computationally expensive or they have too many parameters extracted from the imaging data [29].

Even with the power of deep neural networks [30], efficiently modeling tumor growth is non-trivial. The number of deep-learning-based works for the prediction of glioma growth is still limited. To the best of our knowledge, the first to utilize deep learning to model tumor growth, Zhang et al. [31] (2018) used convolutional neural networks to predict pancreatic tumor growth. Their network predicts which voxels will “become tumors” after a predetermined time in a relatively straightforward manner. Gaw et al. [32] (2019) tried to combine a reaction-diffusion model (proliferation-Invasion mechanistic tumor growth model) with a data-driven graph-based semi-supervised learning model to provide spatially resolved tumor cell density predictions on primary glioblastoma patients with pre-operative MRI. The authors of [12] (2020) explored the possibility of using generative adversarial networks (GAN [33]) for predicting pre-operative glioma growth on both high-grade and low-grade. In contrast to the deterministic tumor growth models described above, which predict a single growth estimate, the authors of [11], [13] introduced a deep probabilistic generative model for learning glioma growth dynamics, i.e., estimating a distribution of possible future changes given previous observations of the same tumor. However, the proposed model was neither able

¹In WHO 2021, the entity of glioblastoma will be fully reconceived as an IDH-wild type diffuse astrocytoma by definition [20].

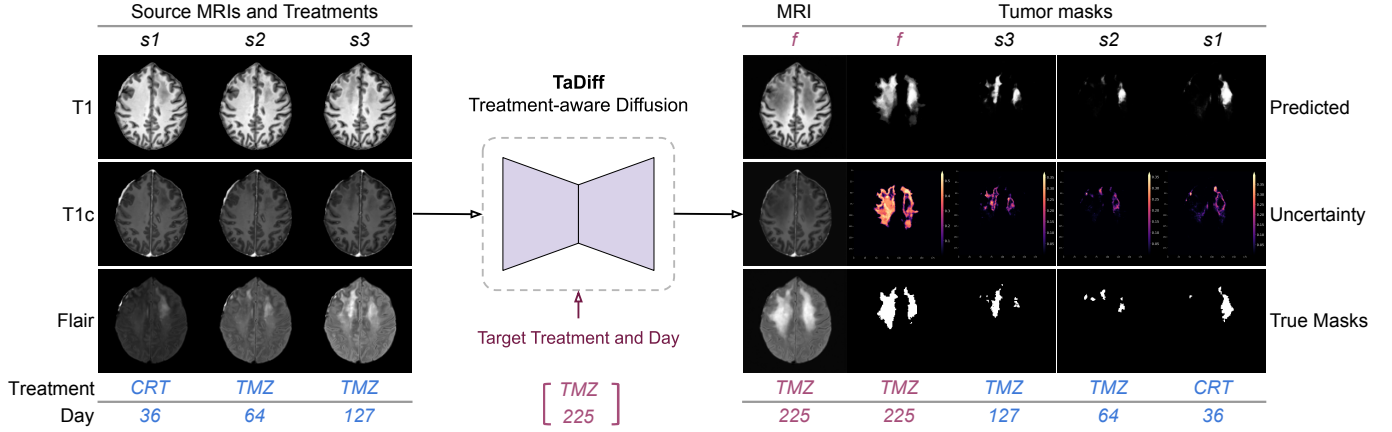


Fig. 2. An overview of the TaDiff model (short for Treatment-aware Diffusion Probabilistic model). The goal of our method is to generate a set of synthetic MRIs and tumor progression masks for any given future time point with source sequential MRIs and treatments. More details are presented in Section IV.

to predict a single correct growth trajectory nor address the spatially varying growth of a tumor.

Recently, the denoising diffusion probabilistic model (DDPM) [16], also known as diffusion model or score-based generative model [15], has shown remarkable performance in (un)conditional image generation [34]–[38] by learning a Markov chain process for the transformation of the simple Gaussian distribution into the data distribution [39]. A growing body of research in the medical image field has also emerged and developed various DDPM-based approaches to successfully address tasks such as tumor segmentation [40], [41], and longitudinal MRI generation [42], [43]. However, to the best of our knowledge, no published work on tumor growth prediction tasks using diffusion models exists so far. Our approach simultaneously models glioma growth using DDPM and generates multi-parametric MRIs. Like [40], applying our model with multiple stochastic sampling processes, one can obtain pixel-wise uncertainty maps for both the predicted tumor masks and the synthesized MRIs.

III. PRELIMINARY

The core ideas of diffusion models [16], [34] can be summarized into two key processes: a forward diffusion process, where noise is added to the data, and a reverse diffusion process where a deep neural network tries to separate the noise from the data.

1) *Forward Diffusion Process*: The forward process is defined as a Markov Chain in which Gaussian noise is gradually added into a data sample \mathbf{x}_0 (e.g. an image) over T successive steps parameterized by a schedule of variances $\{\beta_t \in (0, 1)\}_{t=1}^T$ to produce a sequence of noisy samples $\mathbf{x}_1, \dots, \mathbf{x}_T$. It is described by the formulation:

$$q(\mathbf{x}_{1:T}|\mathbf{x}_0) = \prod_{t=1}^T q(\mathbf{x}_t|\mathbf{x}_{t-1}) \approx \mathcal{N}(\mathbf{0}; \mathbf{I}). \quad (1)$$

At each step of the forward process, Gaussian noise is added according to $q(\mathbf{x}_t|\mathbf{x}_{t-1}) = \mathcal{N}(\mathbf{x}_t; \sqrt{1-\beta_t}\mathbf{x}_{t-1}, \beta_t\mathbf{I})$, where the noisy level is controlled by the variance β_t (known as the

'diffusion rate'). The data sample gradually loses its distinguishable features as the step t becomes larger. Eventually when $T \rightarrow \infty$, \mathbf{x}_T is equivalent to an isotropic Gaussian distribution. A key property of the forward process is that an arbitrary sample from the Markov chain can be obtained without computing each step in the sequence. Let $\alpha_t = 1 - \beta_t$ and $\bar{\alpha}_t = \prod_{i=1}^t \alpha_i$, we can produce a sample $\mathbf{x}_t \sim q(\mathbf{x}_t|\mathbf{x}_0)$ at a timestep t by the formulation.

$$\mathbf{x}_t = \sqrt{\bar{\alpha}_t}\mathbf{x}_0 + \sqrt{1-\bar{\alpha}_t}\boldsymbol{\epsilon}, \quad (2)$$

where $\boldsymbol{\epsilon} \sim \mathcal{N}(\mathbf{0}, \mathbf{I})$. Thus the forward diffusion process can be rewritten/simplified in terms of α as

$$q(\mathbf{x}_t|\mathbf{x}_0) = \mathcal{N}(\mathbf{x}_t; \sqrt{\bar{\alpha}_t}\mathbf{x}_0, (1-\bar{\alpha}_t)\mathbf{I}). \quad (3)$$

2) *Reverse Diffusion Process*: The reverse process is also a Markov chain. In this case, a neural network parameterized by θ predicts the reverse diffusion process at each timestep described as

$$p_\theta(\mathbf{x}_{0:T}) = p(\mathbf{x}_T) \prod_{t=1}^T p_\theta(\mathbf{x}_{t-1}|\mathbf{x}_t), \quad (4)$$

where

$$p_\theta(\mathbf{x}_{t-1}|\mathbf{x}_t) = \mathcal{N}(\mathbf{x}_{t-1}; \boldsymbol{\mu}_\theta(\mathbf{x}_t, t), \boldsymbol{\Sigma}_\theta(\mathbf{x}_t, t)). \quad (5)$$

It is noteworthy that the reverse conditional probability is tractable when conditioned on \mathbf{x}_0 :

$$q(\mathbf{x}_{t-1}|\mathbf{x}_t, \mathbf{x}_0) = \mathcal{N}(\mathbf{x}_{t-1}; \tilde{\boldsymbol{\mu}}_t(\mathbf{x}_t, \mathbf{x}_0), \tilde{\boldsymbol{\beta}}_t\mathbf{I}), \quad (6)$$

where

$$\tilde{\boldsymbol{\mu}}_t(\mathbf{x}_t, \mathbf{x}_0) = \frac{\sqrt{\bar{\alpha}_{t-1}}\beta_t}{1-\bar{\alpha}_t}\mathbf{x}_0 + \frac{\sqrt{\alpha_t}(1-\bar{\alpha}_{t-1})}{1-\bar{\alpha}_t}\mathbf{x}_t, \quad (7)$$

and

$$\tilde{\boldsymbol{\beta}}_t = \frac{1-\bar{\alpha}_{t-1}\beta_t}{1-\bar{\alpha}_t}. \quad (8)$$

Because of $\mathbf{x}_0 = \frac{1}{\sqrt{\bar{\alpha}_t}}(\mathbf{x}_t - \sqrt{1-\bar{\alpha}_t}\boldsymbol{\epsilon}_t)$ (Eq. 2), then

$$\tilde{\boldsymbol{\mu}}_t = \frac{1}{\sqrt{\alpha_t}}\left(\mathbf{x}_t - \frac{1-\alpha_t}{\sqrt{1-\bar{\alpha}_t}}\boldsymbol{\epsilon}_t\right). \quad (9)$$

3) *Training*: For the reverse diffusion process, a neural network is trained to approximate the conditional probability distributions, i.e., train μ_θ to predict $\tilde{\mu}_t$. Because \mathbf{x}_t is available (Eq. 9) as input in training time, it is common to predict ϵ from the input \mathbf{x}_t at time step t , thus

$$\tilde{\mu}_t \approx \mu_\theta(\mathbf{x}_t, t) := \frac{1}{\sqrt{\alpha_t}} \left(\mathbf{x}_t - \frac{1 - \alpha_t}{\sqrt{1 - \alpha_t}} \tilde{\epsilon}_\theta(\mathbf{x}_t, t) \right). \quad (10)$$

By letting $\Sigma_\theta(\mathbf{x}_t, t) = \tilde{\beta}_t \mathbf{I}$, and letting the forward variances β_t to be a sequence of linearly increasing constants from $\beta_1 = 10^{-4}$ to $\beta_T = 0.02$, and some other simplifications in the work [16], we can minimize the MSE loss of the noise to train the neural network.

$$\mathbb{E}_{t \sim [1, T], \mathbf{x}_0, \epsilon} \left[\|\epsilon - \tilde{\epsilon}_\theta(\mathbf{x}_t, t)\|^2 \right]. \quad (11)$$

4) *Inference*: A neural network trained on the reverse diffusion process can be used for generating data. This is achieved by initializing $\mathbf{x}_T \sim \mathcal{N}(\mathbf{0}, \mathbf{1})$ and in T steps, denoise the image, using

$$\mathbf{x}_{t-1} = \frac{1}{\sqrt{\alpha_t}} \left(\mathbf{x}_t - \frac{1 - \alpha_t}{\sqrt{1 - \alpha_t}} \tilde{\epsilon}_\theta(\mathbf{x}_t, t) \right) + \sqrt{\tilde{\beta}_t} \mathbf{z}. \quad (12)$$

where $\mathbf{z} \sim \mathcal{N}(\mathbf{0}, \mathbf{1})$ is new noise added between each denoising step.

IV. METHODS

The classical DDPM approach requires only \mathbf{x}_t for training, resulting in arbitrary images \mathbf{x}_0 when sampling from random noise during inference. However, our goal is not to generate arbitrary images but to generate realistic MRIs and tumor growth maps for any target (future) treatment-day point from a given sequence of source/conditioning images and treatment information. To this end, we propose the treatment-aware diffusion (TaDiff) model for multi-parametric MRI generation and tumor growth prediction on longitudinal data. Our TaDiff model introduces a treatment-aware mechanism for conditioning a diffusion model while also employing a joint learning strategy to segment the tumor and project its future growth during diffusion processes. Figure 3 illustrates an overview of the TaDiff pipeline.

A. Problem Settings

Let tumor binary masks $\mathbf{M} \in \mathbb{R}^{L \times H \times W \times D}$ be a longitudinal 3D tumor volumes with temporal length L . The corresponding longitudinal MRI scans $\mathbf{X} \in \mathbb{R}^{L \times C \times H \times W \times D}$ with C channels. In the current study we consider $C = 3$ due to the availability of three inputs: T1-weighted (T1), contrast-enhanced T1 (T1C), and fluid attenuated inversion recovery (FLAIR) images. The corresponding treatment is denoted by $\mathcal{T} = \{\tau_1, \tau_2, \dots, \tau_l, \dots, \tau_L\}$ and treatment days $\mathcal{D} = \{d_1, d_2, \dots, d_l, \dots, d_L\} \quad \forall d \in \mathbb{N}_0$ and $0 \leq d_{l-1} < d_l$. Note also that in this work, we have only two types of treatments: chemoradiation (CRT) and temozolomide (TMZ), denoted 1 and 2, respectively. We defined $\tau \in \{1, 2\} \sim \mathcal{T}$.

We randomly sample a sorted sequence of three scalar indices from available longitudinal exams as conditional sources, i.e., $\mathcal{S} = \{s_1, s_2, s_3\}$, such that $s_i \in [1, \dots, L - 1]$ and

$s_i \leq s_{i+1}$. Then we sample one scalar index of future (target) session from the rest of future exams, i.e., $f \in [s_3 + 1, \dots, L]$. The set of conditional MRIs from \mathbf{X} is $\mathbf{X}^{\mathcal{S}} \in \mathbb{R}^{3 \times C \times H \times W \times D}$ and set of future/target MRIs is $\mathbf{X}^f \in \mathbb{R}^{1 \times C \times H \times W \times D}$. Correspondingly, we also get source tumor masks $\mathbf{M}^{\mathcal{S}} \in \mathbb{R}^{3 \times H \times W \times D}$ and the future tumor growth mask $\mathbf{M}^f \in \mathbb{R}^{1 \times H \times W \times D}$. As well as the associated sequence of paired treatment and day variables, i.e. $\langle \mathcal{T}, \mathcal{D} \rangle^{\mathcal{S} \cup f} = \{\langle \tau_{s_1}, d_{s_1} \rangle, \langle \tau_{s_2}, d_{s_2} \rangle, \langle \tau_{s_3}, d_{s_3} \rangle, \langle \tau_f, d_f \rangle\}$.

The objective is to maximize the posteriors, $p(\mathbf{M}^f | \mathbf{X}^{\mathcal{S}})$, $p(\mathbf{X}^f | \mathbf{X}^{\mathcal{S}})$, and $p(\mathbf{M}^{\mathcal{S}} | \mathbf{X}^{\mathcal{S}})$, i.e., to predict future tumor masks, generate the future MRIs, and segment the source tumor masks, given the conditional MRIs $\mathbf{X}^{\mathcal{S}}$ with a sequence of paired treatments and days $\langle \mathcal{T}, \mathcal{D} \rangle^{\mathcal{S} \cup f}$. The three posteriors can be combined into a joint probability $p(\mathbf{M}^{\mathcal{S} \cup f}, \mathbf{X}^f | \mathbf{X}^{\mathcal{S}}, \langle \mathcal{T}, \mathcal{D} \rangle^{\mathcal{S} \cup f})$. Due to the computational complexity of the problem, the model training and inference steps are performed using 2D slices sampled along the D dimension of \mathbf{X} and \mathbf{M} , instead of using the 3D imaging volumes, i.e., to maximize the posterior $p(\mathbf{m}^{\mathcal{S} \cup f}, \mathbf{x}^f | \mathbf{x}^{\mathcal{S}}, \langle \mathcal{T}, \mathcal{D} \rangle^{\mathcal{S} \cup f})$, where $\mathbf{m}^{\mathcal{S} \cup f} \in \mathbb{R}^{4 \times H \times W} \sim \mathbf{M}^{\mathcal{S} \cup f}$, $\mathbf{x}^{\mathcal{S}} \in \mathbb{R}^{3 \times C \times H \times W} \sim \mathbf{X}^{\mathcal{S}}$, and $\mathbf{x}^f \in \mathbb{R}^{C \times H \times W} \sim \mathbf{X}^f$.

Algorithm 1: TaDiff Training

1 repeat

// Sample conditional and future MRI data.

Note that we let $|\mathcal{S} \cup f| = 4$ in this work.

2 $(\mathbf{x}^{\mathcal{S} \cup f}, \mathbf{m}^{\mathcal{S} \cup f}, \langle \mathcal{T}, \mathcal{D} \rangle^{\mathcal{S} \cup f}) \sim p(\mathbf{X}, \mathbf{M}, \langle \mathcal{T}, \mathcal{D} \rangle)$

3 $t \sim \text{Uniform}(1, \dots, T)$

4 $\epsilon \sim \mathcal{N}(\mathbf{0}; \mathbf{I})$

// Eq. 2, adding noise into target images

5 $\mathbf{x}_t = \sqrt{\alpha_t} \mathbf{x}^f + \sqrt{1 - \alpha_t} \epsilon$

6 $(\tilde{\epsilon}, \tilde{\mathbf{m}}) = \mu_\theta(\mathbf{x}^{\mathcal{S}} \cup \mathbf{x}_t, \langle \mathcal{T}, \mathcal{D} \rangle^{\mathcal{S} \cup f}, t)$

// Eq. 14, compute the segmentation loss on both source and future tumors

7 $\tilde{\mathbf{m}}^{\mathcal{S}}, \tilde{\mathbf{m}}^f = \text{partition}(\tilde{\mathbf{m}})$

8 $\ell_{seg} = \ell_{dice}(\tilde{\mathbf{m}}^{\mathcal{S}}, \mathbf{m}^{\mathcal{S}}) + \sqrt{\alpha_t} \ell_{dice}(\tilde{\mathbf{m}}^f, \mathbf{m}^f)$

// Computer ω based on Eq. 15

9 Take the joint gradient step according to

$$\nabla_\theta \left(\|\omega(\epsilon - \tilde{\epsilon})\|^2 + \lambda \ell_{seg} \right)$$

10 until converged

B. Treatment-aware Diffusion Network

We used a backbone neural network similar to the classical UNet-based diffusion models introduced by Ho et al. [34]. The timesteps of the diffusion process are encoded into the neural network using sinusoidal embedding [44] and a single-layer multilayer perceptron (MLP). Following the timesteps embedding idea, we utilize two separate embedding and MLP layers for injecting the paired treatment and day information (i.e., $\langle \tau_{s_1}, d_{s_1} \rangle, \langle \tau_{s_2}, d_{s_2} \rangle, \langle \tau_{s_3}, d_{s_3} \rangle$, and $\langle \tau_f, d_f \rangle$) into our network. Specifically, the four pairs of treatment and day are sequentially fed into the two embedding MLP layers

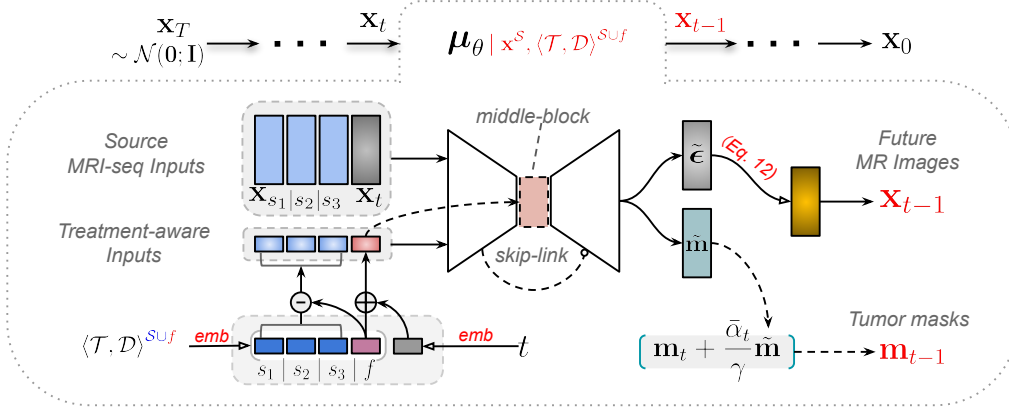


Fig. 3. TaDiff model end-to-end pipeline for multi-parametric MRI generation and tumor growth prediction with respect to any given treatment information and target/future time point. In general, the model takes both conditioning source MRI sequences and treatment-aware embeddings as input, outputs target/future MRIs, and predicts tumor masks for both source treatment-day points and the given target treat-day point at the same time. Section IV-B presents more details about the network architecture, and, algorithms 1 and 2 show details for training and inference with TaDiff model.

Algorithm 2: TaDiff Sampling/inference

Input: Source images: \mathbf{x}^S , source and target (future) treatment-day $\langle \mathcal{T}, \mathcal{D} \rangle^{SUF}$

Output: Future MRI: \mathbf{x}^f and tumor masks: \mathbf{m}^{SUF}

// $T=600$ and $T_m=10$ as default

- 1 Initialize diffusion steps T and mask fusion steps T_m
 - 2 Initialize $\mathbf{x}_T \sim \mathcal{N}(\mathbf{0}; \mathbf{I}) \in \mathbb{R}^{3 \times H \times W}$
 - 3 Initialize $\mathbf{m}_{T_m} \leftarrow \mathbf{0} \in \mathbb{R}^{4 \times H \times W}$
 - // Computer tumor mask fusion factor.
 - 4 $\gamma = \sum_{t=1}^{T_m} \bar{\alpha}_t$
 - 5 **for** $t \leftarrow T, \dots, 1$ **do**
 - 6 $z \sim \mathcal{N}(\mathbf{0}; \mathbf{I})$ **if** $t > 1$ **else** $z = \mathbf{0}$
 - 7 $(\tilde{\epsilon}, \tilde{\mathbf{m}}) = \mu_\theta(\mathbf{x}^S \cup \mathbf{x}_t, \langle \mathcal{T}, \mathcal{D} \rangle^{SUF}, t)$
 // Eq. 12 denoising.
 - 8 $\mathbf{x}_{t-1} = \frac{1}{\sqrt{\alpha_t}} \left(\mathbf{x}_t - \frac{1-\alpha_t}{\sqrt{1-\alpha_t}} \tilde{\epsilon} \right) + \sqrt{\beta_t} z$
 // Fuse the last T_m predicted masks
 - 9 $\mathbf{m}_{t-1} = \mathbf{m}_t + \frac{\bar{\alpha}_t}{\gamma} \tilde{\mathbf{m}}$ **if** $t \leq T_m$
 - 10 **end**
 - 11 **return** $\mathbf{x}^f \leftarrow \mathbf{x}_0$, $\mathbf{m}^{SUF} \leftarrow \mathbf{m}_0$
-

and then we sum the learned treatment embedding with its day embedding to get a unique feature vector for each pair of treatment-day variables. This way we get four treatment vectors: three representing source/past treatment information (indicating by s_1, s_2 and s_3) and one (f) representing the target/future treatment information as illustrated in Figure 3.

Based on experimental observations, we noticed that using the relative (difference) distance between source and target treatment times could help to speed up and stabilize training. As a result, we subtracted the source vectors from the target vectors to get their diff-vectors, which we then concatenate with the summation vector of the target treatment feature and timestep embeddings. We finally used the new concatenated embedding instead of the original timestep embedding to feedforward through the U-Net except for the middle-block part as shown in Figure 3. In the middle-block (also known as

bottle-neck) of U-Net, we only inject the summation feature between the timestep and target treatment embeddings. Based on our experimental observation, this way provides us a smooth and fast learning process when blending the target-treatment messages into the diffusion timesteps.

In the input to the model, we concatenated the source multi-parametric MRIs (i.e., $\mathbf{x}_{s_1}, \mathbf{x}_{s_2}$, and, \mathbf{x}_{s_3}) with \mathbf{x}_t . Note that \mathbf{x}_t is the target MRI with diffusion noise according to Eq. 2. There are two outputs of the model. The first is the diffusion estimated diffusion noise at the time step t . This can be used to generate images using Eq. 12. The second output is the prediction of the tumor masks from both the source MRIs (\mathbf{x}^S) and the noised target MRI (\mathbf{x}_t). As a result, rather than being a pure diffusion model, our TaDiff is a hybrid network that combines both denoising diffusion and segmentation tasks, allowing us to generate future MRI and segment longitudinal tumor growth masks simultaneously in an end-to-end manner. We present the extension of the DDPM training and sampling processes in Algorithms 1 and 2 respectively.

The uncertainty maps can be generated by computing the standard deviation of our model's predictions on the same conditioning inputs with multiple samplings (in this work, we considered 5 samplings).

C. Joint Loss Function

Because the model predicts a series of tumor masks on both source and future MRIs in addition to the conventional diffusion noise. We hence employ the dice loss [45], for the segmentation subtask, which is defined as

$$\ell_{dice}(\tilde{\mathbf{m}}, \mathbf{m}) = 1 - \frac{2|\tilde{\mathbf{m}}\mathbf{m}|}{|\tilde{\mathbf{m}}| + |\mathbf{m}|}. \quad (13)$$

where $|\cdot|$ denotes the L_1 norm. Due to the lack of information in \mathbf{x}_t for high t , predicting a good mask from the image is unfeasible for the model. We therefore weigh the Dice loss of the future segmentation according to the weight of \mathbf{x}_0 in \mathbf{x}_t . The segmentation loss is then defined as

$$\ell_{seg} = \ell_{dice}(\tilde{\mathbf{m}}^S, \mathbf{m}^S) + \sqrt{\bar{\alpha}_t} \ell_{dice}(\tilde{\mathbf{m}}^f, \mathbf{m}^f). \quad (14)$$

The first dice loss is used for segmentations ($\tilde{\mathbf{m}}^S$) of the source images, while the second dice loss is scaled/weighted by the noise level factor $\bar{\alpha}$ used for predicting the tumor masks ($\tilde{\mathbf{m}}^f$) of noised target images (\mathbf{x}_t).

In addition, we propose a weighting mechanism that enables the model to prioritize and extract representations from the glioma region and its most dynamic and heterogeneous surrounding regions, preventing the model from directly copying the representations of reference source input images and facilitating future MRI construction task learning. To this end, the weighting function is designed as

$$\omega = \hat{\mathbf{m}}e^{-\hat{\mathbf{m}}} * \mathbf{f}_{k_l \times k_l} + 1. \quad (15)$$

where $\hat{\mathbf{m}} = \sum_{i \in \text{SUf}} \mathbf{m}_{(i, \dots)}^{\text{SUf}}$, $*$ denotes a convolution operation and $\mathbf{f}_{k_l \times k_l}$ is a convolution filter initialized as 0.1 with a predefined kernel size (default as $k_l = 11$). The weights for the dilated tumor growth region will be in the range [5.451, 1.886], while for the other region, the weights will be 1. The weight matrix element value reflects the level to which the corresponding spatial feature has changed over longitudinal time points.

Finally, the joint loss function for training the TaDiff model is defined as

$$\ell_{\text{TaDiff}} = \|\omega(\epsilon - \tilde{\epsilon})\|^2 + \lambda \ell_{\text{seg}}. \quad (16)$$

where λ controls the amount of segmentation loss during the joint optimization training process. Guided by our experiments and observation, we set $\lambda = 0.01$ in this work.

V. EXPERIMENTS

A. Dataset and Metric

A total of 127 MRI exams were used for this study. There were 23 patients with diffuse high-grade glioma, confirmed by histology, and these patients received treatment at our institution [46]. Patients received standard treatment, including surgery, fractionated radiotherapy (approximately four weeks after surgery) with concomitant and/or adjuvant chemotherapy (CRT) with temozolomide (TMZ) [47]. There were between 3 and 19 (mean 10) longitudinal MRI scans acquired, consisting of multi-parametric types (used in this study): pre-contrast T1-weighted, post-contrast T1-weighted (T1c), and T2 fluid-attenuated inversion recovery (Flair). Scans were skull-stripped, registered to a common space defined by the T1, and resampled to isotropic 1 mm resolution. For intensity normalization, we utilized z-score normalization on a per-channel basis (channel means image type, i.e., T1, T1c, Flair, etc). Ground truth segmentations of edema and enhancing tumors were created by experienced neuroradiologists. Figure 1 shows an example of longitudinal glioma evolution with respect to post-operation treatments and days. The dataset was manually divided into two parts, a training/validation set, and a test set. The training set included 18 patients and 177 longitudinal scans, while the test set consisted of 5 representative patients from a wide range of age groups (32–65) with a total of 48 longitudinal scans.

Metric: To evaluate the accuracy of the tumor segmentation and growth predictions, we calculated the Dice Similarity

Coefficient (DSC) and Relative Volume Difference (RVD) between the ground truth annotations and the estimated tumor maps with an optimized threshold. For evaluating the quality of the generated MRIs, three widely used evaluation metrics were utilized, i.e., the structural similarity index (SSIM) [48], peak signal-to-noise ratio (PSNR), and mean squared error (MSE) between the target and the synthesized multi-parametric MRIs.

B. Implementation and Training Details

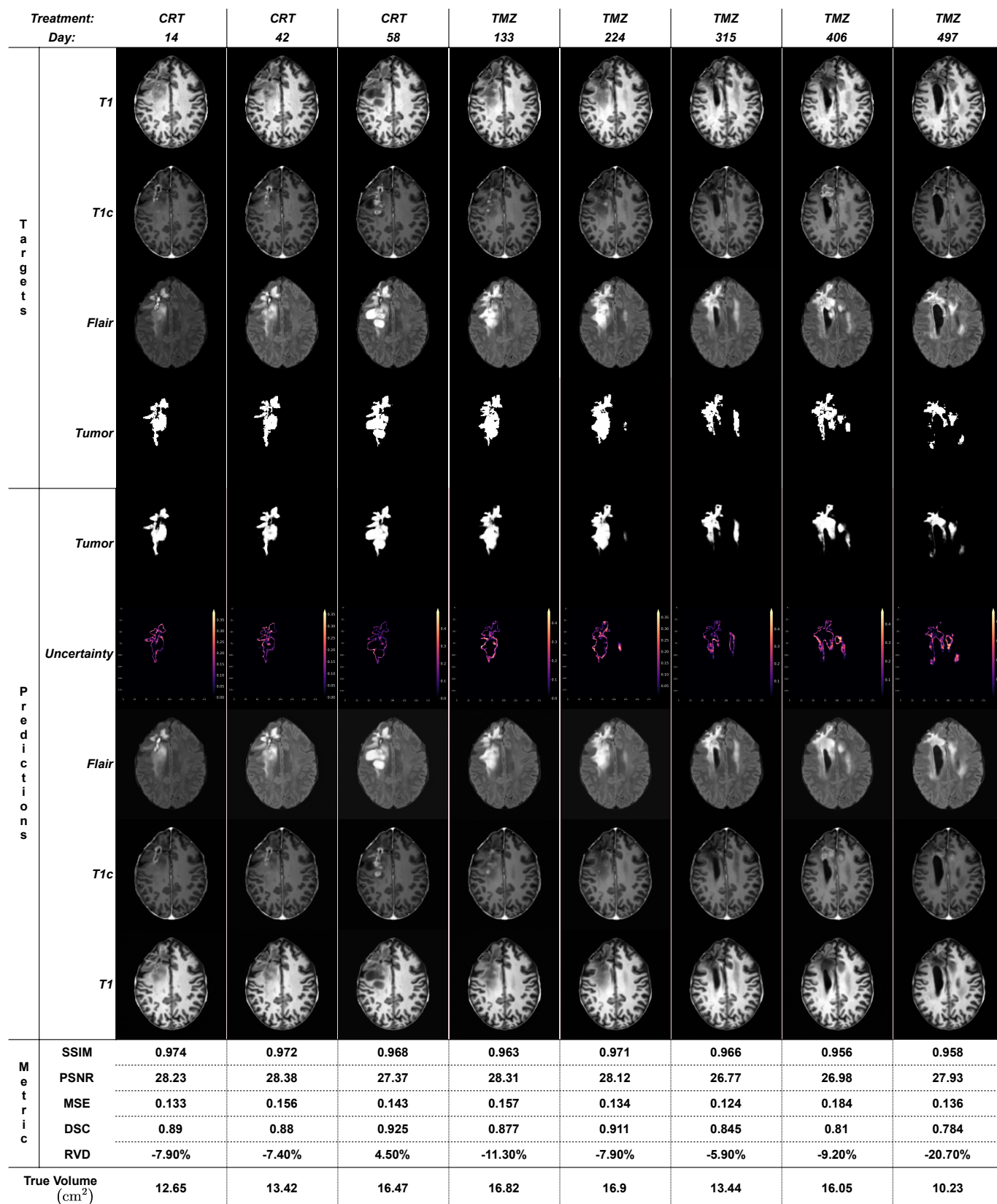
The proposed method was implemented with PyTorch [49]. The model used a 2D UNet-like structure that consists of an encoder and decoder with skip connections and 64, 128, 256, and 512 channels for each stage. For the diffusion module, we modified the network designed in DDPM [34] into our proposed treatment-aware conditioning model. We employed the Adam optimizer algorithm with an initial learning rate 2.5×10^{-4} with a warm-up (1000 steps) and cosine decay scheduler to train the model for 5 million iterations. We used a batch size of 32 and a gradient accumulation step of 2. The images were cropped to a patch size of 192×192 . The training took 350 GPU hours using a single Nvidia V100 32GB GPU.

C. Results and Discussion

We tested our model on the slices containing a tumor of at least 1 cm² at each target session, resulting in a total of 3,352 test slices. Figure 4 illustrates qualitatively and quantitatively the ability of the model to predict future tumor appearances and the corresponding panel of three MR images. The model requires three source MRIs as input; if there are fewer sequences then the most recent source is repeated/duplicated.

In the following two tables, we summarized the results of our model on three tasks: multi-parametric MRI generation, future tumor prediction, and source tumor segmentation, in which \uparrow / \downarrow indicates that higher/lower is better. Table I shows the test performance of each patient (i.e., P-1, P-2, P-3, P-4, and P-5) across various ages (32 – 65 years old) and survival time (11 – 83 months). Table II summarized the results into five treatment-day ranges, i.e., 0 – 50 (about the first 6 weeks of CRT treatment), 51 – 220 (around 24 weeks of TMZ treatment in 6 cycles), 221 – 365 (one-year survival), 366 – 720 (two-year survival), and 721+ (over two-year survival). Overall, we observed that the model is able to account for stable and progressive tumor cases with growth and shrinkage in different locations. Figure 5 shows the qualitative comparisons of the predictions from our model and the ground truth on the test set.

For multi-parametric MRI generation tasks, our model demonstrated high performance with average SSIM: 0.919 ± 0.03 , PSNR: 27.9 ± 1.2 , and MSE: 0.174 ± 0.05 . Figure 6 compares the generation metric’s distributions regarding each treatment (CRT and TMZ) for each patient. It’s worth noticing that TMZ has a long-tail distribution below the first quartile for patients (P-1 and P-2) with SSIM (Dashed lines represent the quartiles for each group), whereas CRT has relatively stable distributions across all patients and metrics. In Table II, we also observed the reduced performance (SSIM: 0.877) in the treatment-day range of 221 – 365. We think this is due to two



SSIM: Structural Similarity Index Measure , PSNR: Peak Signal-to-Noise Ratio, MSE: Mean Squared Error, DSC: Dice Similarity Coefficient, RVD: Relative Volume Difference

Fig. 4. An example of evaluation on a patient from its 1st session to the last session with variable treatment and day protocols. The top four rows of images are the ground truth at each session, the lower rows are the predictions of the TaDiff Model followed by quantitative evaluation metrics. Note that the uncertainty maps were created by computing the standard deviation of our model's predictions on input images with 5 samplings.

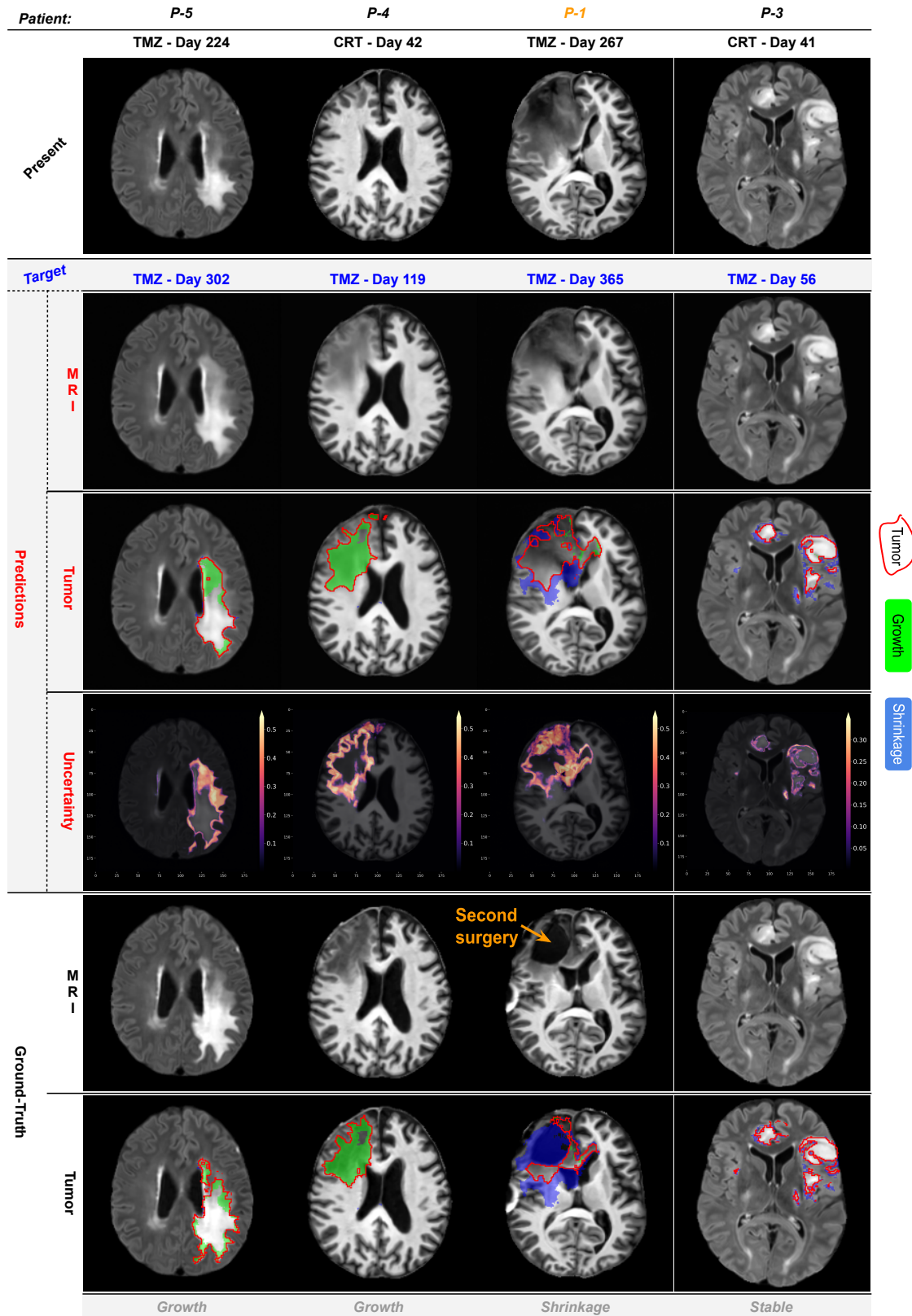


Fig. 5. Examples of qualitative prediction on the test cases. From top to bottom, the Present (source) MRIs with specific treatment-day traces, the Target (future) treatment-day, the Predictions (including generated MRIs, Tumor masks, and Uncertainty maps), and the Ground truth. The method can model both stable and progressive tumors with growth and shrinkage in different spots. Note that P-1 had a second surgery treatment which was beyond the range of treatment types our model was designed to handle.

TABLE I
RESULTS ON EACH TEST PATIENT.

Patient ID	Age	Survival-month	Multi-parametric MRI Generation			Future Tumor Prediction		Source Tumor Segmentation	
			SSIM \uparrow	PSNR \uparrow	MSE \downarrow	DSC \uparrow	RVD \downarrow	DSC \uparrow	RVD \downarrow
^a P-1	32	84	0.886 \pm 0.06	28.141 \pm 1.30	0.155 \pm 0.05	0.691 \pm 0.16	0.139 \pm 0.69	0.828 \pm 0.09	0.087 \pm 0.18
^b P-2	44	19	0.926 \pm 0.04	28.479 \pm 1.76	0.138 \pm 0.05	0.578 \pm 0.17	0.415 \pm 1.61	0.818 \pm 0.08	0.053 \pm 0.19
P-3	53	11	0.943 \pm 0.01	27.568 \pm 0.84	0.212 \pm 0.05	0.812 \pm 0.06	-0.191 \pm 0.10	0.893 \pm 0.04	-0.020 \pm 0.08
P-4	64	13	0.903 \pm 0.03	27.668 \pm 0.84	0.197 \pm 0.04	0.757 \pm 0.16	-0.187 \pm 0.24	0.849 \pm 0.16	-0.036 \pm 0.24
P-5	65	40	0.936 \pm 0.03	27.975 \pm 1.24	0.166 \pm 0.05	0.755 \pm 0.10	-0.058 \pm 0.31	0.857 \pm 0.06	0.033 \pm 0.25
Average	52	33	0.919 \pm 0.03	27.966 \pm 1.20	0.174 \pm 0.05	0.719 \pm 0.13	0.024 \pm 0.59	0.849 \pm 0.09	0.023 \pm 0.19

^a P-1 underwent a second surgery treatment to remove glioblastomas between days 267 and 365.

^b P-2 was diagnosed with secondary glioblastomas; such patients were fairly rare (2 cases) in our training dataset.

TABLE II
QUANTITATIVE RESULTS W.R.T TREATMENT DAYS.

Treatment Days	Multi-parametric MRI Generation			Future Tumor Prediction		Source Tumor Segmentation	
	SSIM \uparrow	PSNR \uparrow	MSE \downarrow	DSC \uparrow	RVD \downarrow	DSC \uparrow	RVD \downarrow
0 - 50	0.928 \pm 0.02	27.924 \pm 1.19	0.182 \pm 0.06	0.759 \pm 0.12	-0.133 \pm 0.27	0.858 \pm 0.09	-0.012 \pm 0.17
51 - 220	0.896 \pm 0.07	27.984 \pm 1.36	0.175 \pm 0.06	0.718 \pm 0.16	0.113 \pm 0.71	0.863 \pm 0.08	0.067 \pm 0.19
221 - 365	0.877 \pm 0.06	28.096 \pm 1.38	0.163 \pm 0.05	0.604 \pm 0.20	0.539 \pm 1.68	0.843 \pm 0.10	0.104 \pm 0.39
366 - 720	0.926 \pm 0.03	28.106 \pm 1.33	0.154 \pm 0.05	0.697 \pm 0.14	-0.024 \pm 0.38	0.831 \pm 0.08	0.059 \pm 0.14
721+	0.941 \pm 0.02	28.106 \pm 1.36	0.149 \pm 0.05	0.760 \pm 0.09	-0.012 \pm 0.27	0.830 \pm 0.06	0.039 \pm 0.12

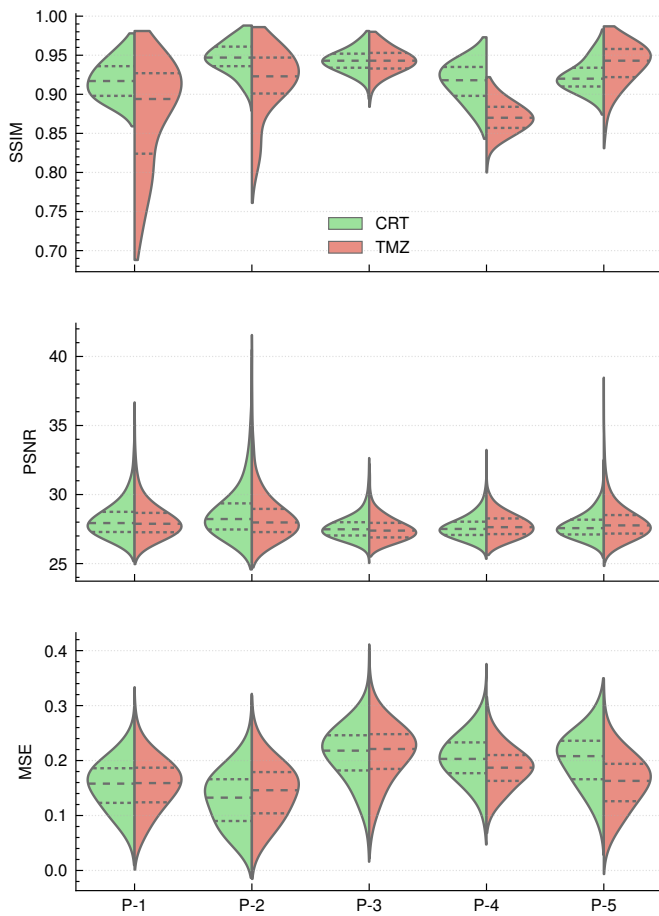


Fig. 6. The three split violin plots compare MRI generation metric's distributions of each treatment (CRT and TMZ) overall patients. Dashed lines represent the quartiles for each group. Notice that TMZ has a long-tail distribution below the first quartile for patients P-1 and P-2 w.r.t SSIM. The main reason is that P-1 was given a second surgery treatment during the TMZ period, and P-2 was diagnosed with a glioma classified as secondary glioblastoma.

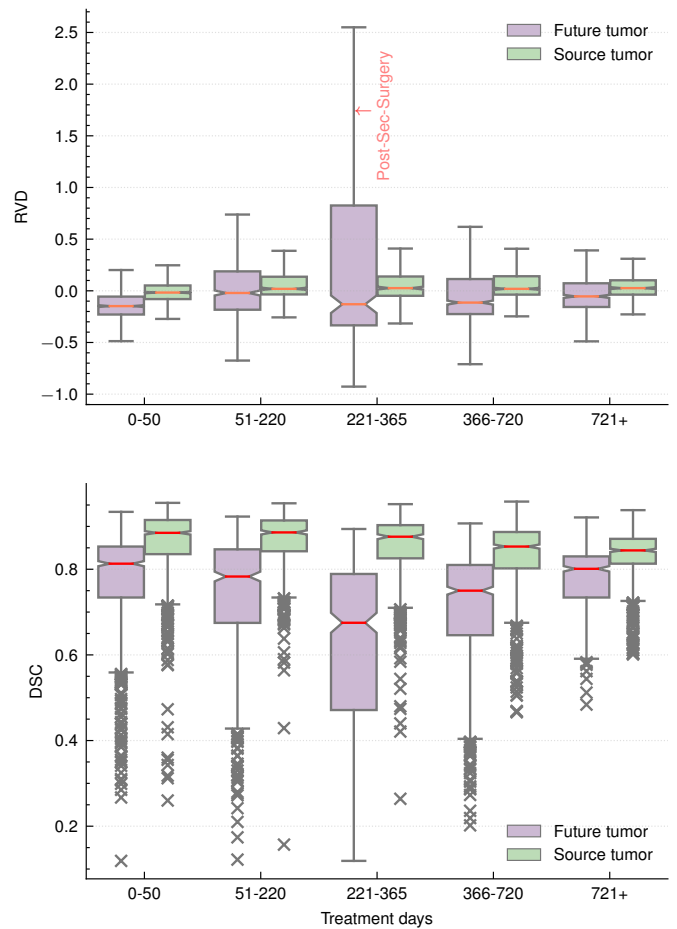


Fig. 7. The two box plots show the RVD and DSC distributions for predicted Future tumors and source tumors across different treatment day ranges. Note that the model's performance reduced significantly with more variances in the day range 221-365, this is because one case (P-1) experienced unusual and rapid glioma growth and underwent a second surgery treatment during this period.

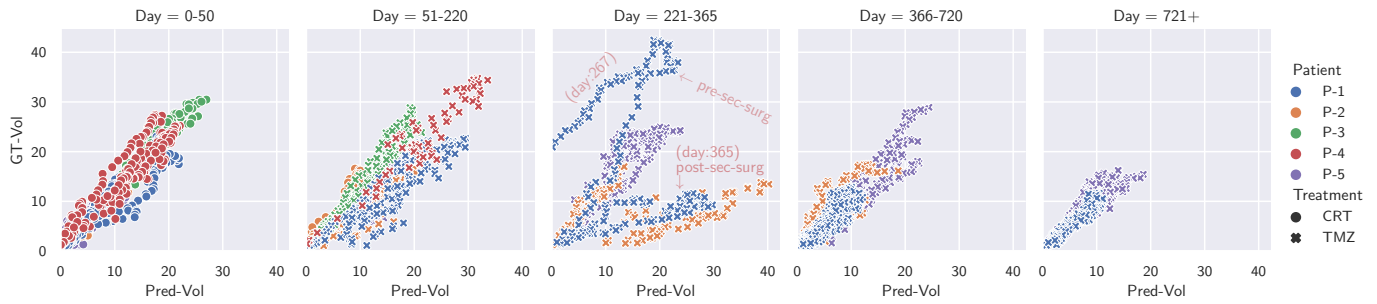


Fig. 8. Tumor growth prediction evaluation in terms of slice-based volume (cm^2) estimation for future treatment and days. This figure shows the detailed relations between GT-Vol and Pred-Vol on each of the day ranges, test patients, and treatment types. Each relational plot corresponds to a target day range, and the patients are differentiated by colors, with different markers indicating the treatment type. Note that We did not filter out cases of the second surgery (pre and post) in these plots, instead illustrating them with annotations on the day=221-365 plot.

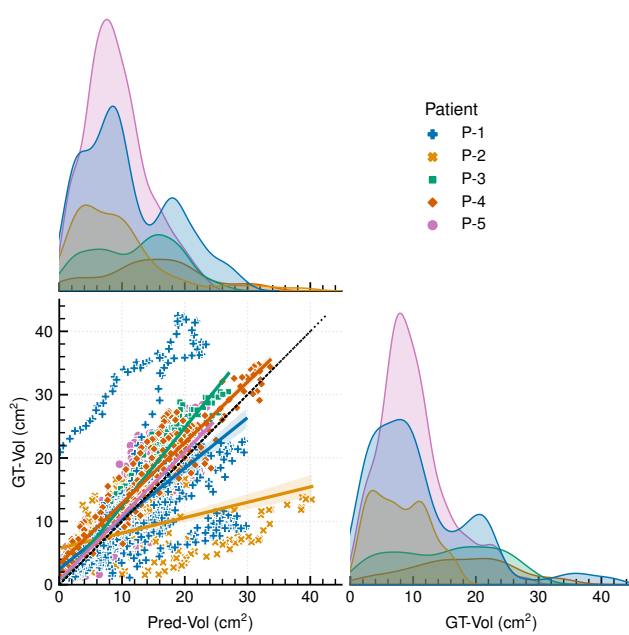


Fig. 9. Tumor growth prediction evaluation on each patient with a paired plot between GT-Vol and Pred-Vol. The plot's identity line indicates the Pred-Vol should ideally equal GT-Vol, and the two distributions of GT-Vol and Pred-Vol reveal their similarities.

factors: first, P-1 had a second surgery treatment on day-365, which was beyond the capability bound of our trained model with only two treatment types, and second, P-2 was diagnosed with secondary glioblastomas, which is a fairly uncommon case in our training set, so our model couldn't predict well on such cases.

Regarding future tumor prediction and source tumor segmentation tasks, the model achieves an overall DSC of 0.719 ± 0.13 and 0.849 ± 0.09 respectively. We also noticed that unknown treatment type (e.g. second surgery on P-1) and uncommon glioma type (e.g. secondary glioblastoma of P-2) had a significant impact on the model's prediction of tumor growth. Patients (P-3-4-5) with primary glioblastomas taking standard treatments (CRT/TMZ) obtained better tumor growth prediction than other patients (P-1-2) (ref to Table I), and the treatment-day range of 221 – 365 is the most difficult time spot for predicting tumor progression among all treatment

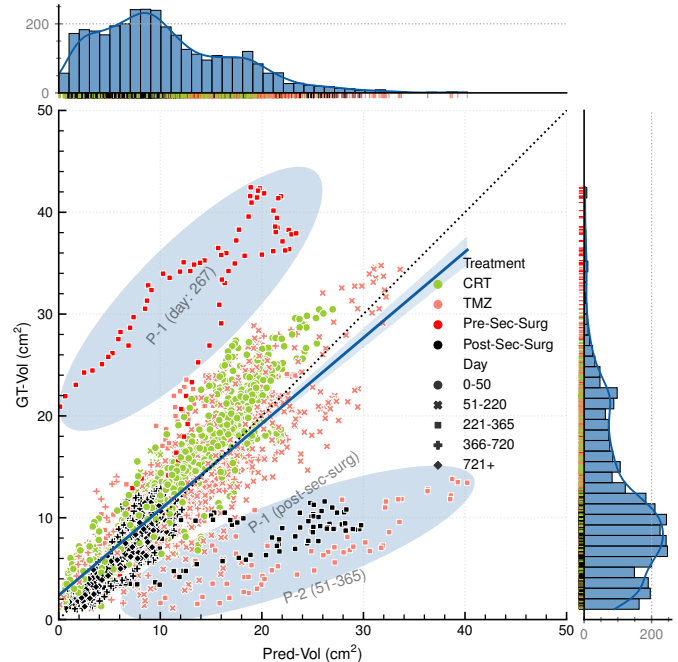


Fig. 10. Tumor growth prediction evaluation based on treatment variables including CRT, TMZ, Second-Surgery (divided into Pre-Sec-Surg and Post-Sec-Surg), as well as their corresponding day ranges. The treatment types are marked by different colors, and the day ranges are indicated by various markers. Two ellipses with annotation texts highlight two outlier regions.

days (ref to Table II). Figure 7 illustrates the distributions of RVD and DSC for predicted future tumor and source tumor respectively across different grouped treatment days. Note that outliers of RVD are not shown for simplicity and better visualization reasons, whereas outliers for DSC are shown as marker 'x'. We also illustrate pair correlation distributions of GT-Vol (short for the ground-truth future tumor volume on a slice), and Pred-Vol (short for predicted future tumor volume) across all test patients on different treatments and day ranges in Figure 8, 9 and 10. From these figures, it can be seen that:

- GT-Vol and Pred-Vol have a similar distribution with similar mean and variance on each test patient with a strong positive correlation, and the overall slope of the regression line (Figure 9), is close to 1, indicating that there is a good growth prediction that matches ground-

truth in general, whereas Figure 9 and 10 show that P-2 has over-predictions on tumor growth during TMZ treatment days 51-365, and P-1 has significantly more outliers than most other patients, e.g., under-prediction on day 267 (gt-vol greater than pred-vol), and over-prediction on day 365 (pred-vol greater than gt-vol).

- The treatment CRT has more points concentrated around the regression line than the TMZ treatment, which has more scattered points with some obvious outliers. Particularly for patients P-1 and P-2, see Figure 8 and 9, there are more outliers in 221-365 and 366-720 day ranges, indicating that the tumor growth prediction becomes worse, which also suggests that the two patients had some abnormal changes or interventions during this period. In this work, we know the possible reason is that, for P-1, the patient had a second surgery on days 267-365 during the TMZ course, whereas for P-2, the patient at the time of diagnosis was classified as secondary glioblastoma. This is why we specifically show an additional treatment variable in Figure 9 i.e., the second surgery, which is divided into Pre-Sec-Surg (short for pre-second-surgery) and Post-Sec-Surg (short for post-second-surgery). However, our current model was trained only on two treatment types (CRT and TMZ) and assumed there is no second surgery intervention during both CRT and TMZ courses.

Outliers: Upon inspection, we noted that the vast majority of poor predictions were concentrated on patients P-1 and P-2 in TMZ treatment day range of 221–365 as shown in Figure 8. These patients, P-1 (33 years old) and P-2 (44 years old), were relatively young, the glioma growth pattern for young patients might be more uncertain in the 221 – 365 day range than for old patients (above 50 years old). For example, P-1’s tumor grew at a rapid rate shown in the 267-day MR exam, which exceeded the mean distribution predicted by our model, as shown in Figure 9. P-2 had secondary glioblastoma² rather than primary glioblastoma, which is common in young patients but fairly rare (2 cases) in our training dataset. This helps to explain why the model over-predicted the tumor’s growth on P-2 i.e. many Pred-Vol are larger than GT-Vol as shown in Figure 8 and 10. Furthermore, our current model can only predict well the tumor growth based on CRT or TMZ treatment with the assumption that there are no other types of interventions (such as second surgery). Because the current model has no way of knowing or estimating which part of the tumor was removed by the second surgery, resulting in our model giving over-prediction on P-1 i.e. Pred-Vol is well larger than GT-Vol after P-1 underwent a second surgery (Post-Sec-Surg) shown in Figure 8 and 9. We believe that as more training cases with secondary glioblastomas become available in the future, our model will perform better and more robustly on such patients as P-2. If we can collect enough cases with

second surgeries, our model can also be easily extended to include more than three treatments (such as CRT, TMZ, and Surgery) rather than two (just CRT/TMZ) as it is now.

Limitations: Our work has some limitations that are discussed herein. First, as a data-driven deep-learning-based method, the model requires more data than methods based on explicit biological diffusion models. The current sample is not sufficient to capture all possible tumor growth or shrinkage patterns related to various diffuse glioma types (such as primary or secondary glioblastomas³) and treatment protocols (such as CRT, and TMZ with or without second surgery), and the test set of 5 subjects is relatively small, hence a larger sample is needed for more extensive evaluation. This is also one of the main reasons why we chose to work on 2D models rather than 3D models, as the latter would significantly reduce the number of available training and test samples. Second, it is important to note that the high computational cost and slow inference/sampling process of DDPM models, which need large batch sizes and hundreds of diffusion steps. To speed up the inference process, future work could be directed to improve sampling methods such as DPM-Solver [51]. Additionally, while our results are promising, the clinical utility of our model needs to be further fine-tuned and validated on larger and more diverse datasets from multiple sites. We are confident that larger datasets will become available in the future, which will enable us to further improve the robustness and accuracy of our method.

VI. CONCLUSIONS

We present a treatment-aware diffusion model for generating longitudinal multi-parametric MRI and predicting diffuse glioma tumor growth. The proposed method employs an optimized joint learning strategy that incorporates a sequence of source MRI and treatment information as conditioning inputs to DDPM, allowing for the generation of future MRI as well as the prediction of series tumor masks on the source and generated MRI. Our model also enables the implicit ensemble of multiple predictions using the stochastic sampling process and further produces uncertainty maps by calculating the variance of these predictions. Thus, this approach has the potential to both predict future tumor growth patterns and quantify tumor evolution uncertainty, thereby improving treatment planning and, ultimately, patient outcomes.

ACKNOWLEDGMENT

The authors want to thank the Digital Research Alliance of Canada for providing free computing resources, and cloud accounts. The authors would also like to thank all of the reviewers (whether anonymous or not) for their insightful comments and careful reading of the manuscript.

²According to [50], secondary glioblastomas progress from low-grade diffuse astrocytoma or anaplastic astrocytoma, which manifest in younger patients, typically with less necrosis, are preferentially located in the frontal lobe, and carry a significantly better prognosis. Despite a similar histologic appearance, primary and secondary glioblastomas are distinct tumor entities that originate from different precursor cells and may require different therapeutic approaches.

³Many tumor types are being phased out of the WHO 5th edition of diffusion glioma classification [20], including primary and secondary glioblastomas. We are still using them in this work, primarily to align with the diagnostic taxonomy from our dataset, as well as many existing related literature.

REFERENCES

- [1] D. N. Louis, A. Perry, P. Wesseling, D. J. Brat, I. A. Cree, D. Figarella-Branger, C. Hawkins, H. Ng, S. M. Pfister, G. Reifenberger, *et al.*, "The 2021 WHO classification of tumors of the central nervous system: a summary," *Neuro-oncology*, vol. 23, no. 8, pp. 1231–1251, 2021.
- [2] J. A. Schwartzbaum, J. L. Fisher, K. D. Aldape, and M. Wrensch, "Epidemiology and molecular pathology of glioma," *Nature clinical practice Neurology*, vol. 2, no. 9, pp. 494–503, 2006.
- [3] R. Stupp, M. E. Hegi, W. P. Mason, M. J. Van Den Bent, M. J. Taphoorn, R. C. Janzer, S. K. Ludwin, A. Allgeier, B. Fisher, K. Belanger, *et al.*, "Effects of radiotherapy with concomitant and adjuvant temozolomide versus radiotherapy alone on survival in glioblastoma in a randomised phase III study: 5-year analysis of the eortc-ncic trial," *The lancet oncology*, vol. 10, no. 5, pp. 459–466, 2009.
- [4] A. E. Zade, S. S. Haghghi, and M. Soltani, "A neuro evolutionary algorithm for patient calibrated prediction of survival in glioblastoma patients," *Journal of Biomedical Informatics*, vol. 115, p. 103694, 2021.
- [5] K. R. Swanson, E. C. Alvord Jr, and J. Murray, "Quantifying efficacy of chemotherapy of brain tumors with homogeneous and heterogeneous drug delivery," *Acta biotheoretica*, vol. 50, no. 4, pp. 223–237, 2002.
- [6] B. H. Menze, K. Van Leemput, A. Honkela, E. Konukoglu, M.-A. Weber, N. Ayache, and P. Golland, "A generative approach for image-based modeling of tumor growth," in *Information Processing in Medical Imaging: 22nd International Conference, IPMI 2011, Kloster Irsee, Germany, July 3-8, 2011. Proceedings 22*, pp. 735–747, Springer, 2011.
- [7] C. Engwer, T. Hillen, M. Knappitsch, and C. Surulescu, "Glioma follow white matter tracts: a multiscale dti-based model," *Journal of mathematical biology*, vol. 71, pp. 551–582, 2015.
- [8] I. Ezhov, J. Lipkova, S. Shit, F. Kofler, N. Collomb, B. Lemasson, E. Barbier, and B. Menze, "Neural parameters estimation for brain tumor growth modeling," in *Medical Image Computing and Computer Assisted Intervention–MICCAI 2019: 22nd International Conference, Shenzhen, China, October 13–17, 2019, Proceedings, Part II 22*, pp. 787–795, Springer, 2019.
- [9] S. Subramanian, K. Scheufele, N. Himthani, and G. Biros, "Multiatlas calibration of biophysical brain tumor growth models with mass effect," in *Medical Image Computing and Computer Assisted Intervention–MICCAI 2020: 23rd International Conference, Lima, Peru, October 4–8, 2020, Proceedings, Part II 23*, pp. 551–560, Springer, 2020.
- [10] D. A. Hormuth, K. A. Al Feghali, A. M. Elliott, T. E. Yankeelov, and C. Chung, "Image-based personalization of computational models for predicting response of high-grade glioma to chemoradiation," *Scientific reports*, vol. 11, no. 1, p. 8520, 2021.
- [11] J. Petersen, F. Isensee, G. Köhler, P. F. Jäger, D. Zimmerer, U. Neuberger, W. Wick, J. Debus, S. Heiland, M. Bendszus, *et al.*, "Continuous-time deep glioma growth models," in *Medical Image Computing and Computer Assisted Intervention–MICCAI 2021: 24th International Conference, Strasbourg, France, September 27–October 1, 2021, Proceedings, Part III 24*, pp. 83–92, Springer, 2021.
- [12] A. Elazab, C. Wang, S. J. S. Gardezi, H. Bai, Q. Hu, T. Wang, C. Chang, and B. Lei, "Gp-gan: Brain tumor growth prediction using stacked 3d generative adversarial networks from longitudinal mr images," *Neural Networks*, vol. 132, pp. 321–332, 2020.
- [13] J. Petersen, P. F. Jäger, F. Isensee, S. A. Kohl, U. Neuberger, W. Wick, J. Debus, S. Heiland, M. Bendszus, P. Kickingereder, *et al.*, "Deep probabilistic modeling of glioma growth," in *Medical Image Computing and Computer Assisted Intervention–MICCAI 2019: 22nd International Conference, Shenzhen, China, October 13–17, 2019, Proceedings, Part II 22*, pp. 806–814, Springer, 2019.
- [14] J. Sohl-Dickstein, E. Weiss, N. Maheswaranathan, and S. Ganguli, "Deep unsupervised learning using nonequilibrium thermodynamics," in *International conference on machine learning*, pp. 2256–2265, PMLR, 2015.
- [15] Y. Song and S. Ermon, "Generative modeling by estimating gradients of the data distribution," *Advances in neural information processing systems*, vol. 32, 2019.
- [16] J. Ho, A. Jain, and P. Abbeel, "Denoising Diffusion Probabilistic Models," *Advances in Neural Information Processing Systems*, vol. 33, pp. 6840–6851, 2020.
- [17] D. P. Kingma and M. Welling, "Auto-encoding variational bayes," *arXiv preprint arXiv:1312.6114*, 2013.
- [18] D. J. Rezende, S. Mohamed, and D. Wierstra, "Stochastic backpropagation and approximate inference in deep generative models," in *International conference on machine learning*, pp. 1278–1286, PMLR, 2014.
- [19] O. Ronneberger, P. Fischer, and T. Brox, "U-Net: Convolutional Networks for Biomedical Image Segmentation," in *Medical Image Computing and Computer-Assisted Intervention–MICCAI 2015: 18th International Conference, Munich, Germany, October 5-9, 2015, Proceedings, Part III 18*, pp. 234–241, Springer, 2015.
- [20] A. Perez and J. T. Huse, "The evolving classification of diffuse gliomas: World health organization updates for 2021," *Current neurology and neuroscience reports*, vol. 21, pp. 1–10, 2021.
- [21] J. Petersen, *Learning Distributions of Functions on a Continuous Time Domain*. PhD thesis, Heidelberg University, 2020.
- [22] O. Clatz, M. Sermesant, P.-Y. Bondiau, H. Delingette, S. K. Warfield, G. Malandain, and N. Ayache, "Realistic simulation of the 3-d growth of brain tumors in mr images coupling diffusion with biomechanical deformation," *IEEE transactions on medical imaging*, vol. 24, no. 10, pp. 1334–1346, 2005.
- [23] H. L. Harpold, E. C. Alvord Jr, and K. R. Swanson, "The evolution of mathematical modeling of glioma proliferation and invasion," *Journal of Neuropathology & Experimental Neurology*, vol. 66, no. 1, pp. 1–9, 2007.
- [24] D. A. Hormuth II, J. A. Weis, S. L. Barnes, M. I. Miga, E. C. Rericha, V. Quaranta, and T. E. Yankeelov, "Predicting in vivo glioma growth with the reaction diffusion equation constrained by quantitative magnetic resonance imaging data," *Physical biology*, vol. 12, no. 4, p. 046006, 2015.
- [25] C. Hoge, C. Davatzikos, and G. Biros, "An image-driven parameter estimation problem for a reaction–diffusion glioma growth model with mass effects," *Journal of mathematical biology*, vol. 56, pp. 793–825, 2008.
- [26] J. T. Oden, E. E. Prudencio, and A. Hawkins-Daarud, "Selection and assessment of phenomenological models of tumor growth," *Mathematical Models and Methods in Applied Sciences*, vol. 23, no. 07, pp. 1309–1338, 2013.
- [27] K. C. Wong, R. M. Summers, E. Kebebew, and J. Yao, "Tumor growth prediction with reaction-diffusion and hyperelastic biomechanical model by physiological data fusion," *Medical Image Analysis*, vol. 25, no. 1, pp. 72–85, 2015.
- [28] J. T. Oden, E. A. Lima, R. C. Almeida, Y. Feng, M. N. Rylander, D. Fuentes, D. Faghihi, M. M. Rahman, M. DeWitt, M. Gadde, *et al.*, "Toward predictive multiscale modeling of vascular tumor growth: computational and experimental oncology for tumor prediction," *Archives of Computational Methods in Engineering*, vol. 23, pp. 735–779, 2016.
- [29] B. Tuñç, D. A. Hormuth II, G. Biros, and T. E. Yankeelov, "Modeling of glioma growth with mass effect by longitudinal magnetic resonance imaging," *IEEE Transactions on Biomedical Engineering*, vol. 68, no. 12, pp. 3713–3724, 2021.
- [30] Y. LeCun, Y. Bengio, and G. Hinton, "Deep learning," *nature*, vol. 521, no. 7553, pp. 436–444, 2015.
- [31] L. Zhang, L. Lu, R. M. Summers, E. Kebebew, and J. Yao, "Convolutional invasion and expansion networks for tumor growth prediction," *IEEE transactions on medical imaging*, vol. 37, no. 2, pp. 638–648, 2017.
- [32] N. Gaw, A. Hawkins-Daarud, L. S. Hu, H. Yoon, L. Wang, Y. Xu, P. R. Jackson, K. W. Singleton, L. C. Baxter, J. Eschbacher, *et al.*, "Integration of machine learning and mechanistic models accurately predicts variation in cell density of glioblastoma using multiparametric mri," *Scientific reports*, vol. 9, no. 1, p. 10063, 2019.
- [33] I. Goodfellow, J. Pouget-Abadie, M. Mirza, B. Xu, D. Warde-Farley, S. Ozair, A. Courville, and Y. Bengio, "Generative adversarial nets," *Advances in neural information processing systems*, vol. 27, 2014.
- [34] P. Dhariwal and A. Nichol, "Diffusion Models Beat GANs on Image Synthesis," *Advances in Neural Information Processing Systems*, vol. 34, pp. 8780–8794, 2021.
- [35] A. Nichol, P. Dhariwal, A. Ramesh, P. Shyam, P. Mishkin, B. McGrew, I. Sutskever, and M. Chen, "Glide: Towards photorealistic image generation and editing with text-guided diffusion models," *arXiv preprint arXiv:2112.10741*, 2021.
- [36] A. Ramesh, P. Dhariwal, A. Nichol, C. Chu, and M. Chen, "Hierarchical text-conditional image generation with clip latents," *arXiv preprint arXiv:2204.06125*, 2022.
- [37] R. Rombach, A. Blattmann, D. Lorenz, P. Esser, and B. Ommer, "High-resolution image synthesis with latent diffusion models," in *Proceedings of the IEEE/CVF conference on computer vision and pattern recognition*, pp. 10684–10695, 2022.
- [38] C. Saharia, W. Chan, S. Saxena, L. Li, J. Whang, E. L. Denton, K. Ghasemipour, R. Gontijo Lopes, B. Karagol Ayan, T. Salimans, *et al.*, "Photorealistic text-to-image diffusion models with deep language

- understanding,” *Advances in Neural Information Processing Systems*, vol. 35, pp. 36479–36494, 2022.
- [39] J. Song, C. Meng, and S. Ermon, “Denoising diffusion implicit models,” *arXiv preprint arXiv:2010.02502*, 2020.
- [40] J. Wolleb, R. Sandkühler, F. Bieder, P. Valmaggia, and P. C. Cattin, “Diffusion models for implicit image segmentation ensembles,” in *International Conference on Medical Imaging with Deep Learning*, pp. 1336–1348, PMLR, 2022.
- [41] A. Rahman, J. M. J. Valanarasu, I. Hacihaliloglu, and V. M. Patel, “Ambiguous medical image segmentation using diffusion models,” in *Proceedings of the IEEE/CVF Conference on Computer Vision and Pattern Recognition*, pp. 11536–11546, 2023.
- [42] B. Kim and J. C. Ye, “Diffusion deformable model for 4d temporal medical image generation,” in *International Conference on Medical Image Computing and Computer-Assisted Intervention*, pp. 539–548, Springer, 2022.
- [43] J. S. Yoon, C. Zhang, H.-I. Suk, J. Guo, and X. Li, “Sadm: Sequence-aware diffusion model for longitudinal medical image generation,” in *International Conference on Information Processing in Medical Imaging*, pp. 388–400, Springer, 2023.
- [44] A. Vaswani, N. Shazeer, N. Parmar, J. Uszkoreit, L. Jones, A. N. Gomez, Ł. Kaiser, and I. Polosukhin, “Attention is all you need,” *Advances in neural information processing systems*, vol. 30, 2017.
- [45] F. Milletari, N. Navab, and S.-A. Ahmadi, “V-net: Fully convolutional neural networks for volumetric medical image segmentation,” in *2016 Fourth International Conference on 3D Vision (3DV)*, pp. 565–571, IEEE, 2016.
- [46] C. Larsson, I. Groote, J. Vardal, M. Kleppstø, A. Odland, P. Brandal, P. Due-Tønnessen, S. S. Holme, T. R. Hope, T. R. Meling, *et al.*, “Prediction of Survival and Progression in Glioblastoma Patients Using Temporal Perfusion Changes During Radiochemotherapy,” *Magnetic Resonance Imaging*, vol. 68, pp. 106–112, 2020.
- [47] E. Fuster-Garcia, I. Thokle Hovden, S. Fløgstad Svensson, C. Larsson, J. Vardal, A. Bjørnerud, and K. E. Emblem, “Quantification of Tissue Compression Identifies High-Grade Glioma Patients with Reduced Survival,” *Cancers*, vol. 14, no. 7, p. 1725, 2022.
- [48] Z. Wang, A. C. Bovik, H. R. Sheikh, and E. P. Simoncelli, “Image Quality Assessment: from Error Visibility to Structural Similarity,” *IEEE Transactions on Image Processing*, vol. 13, no. 4, pp. 600–612, 2004.
- [49] A. Paszke, S. Gross, S. Chintala, G. Chanan, E. Yang, Z. DeVito, Z. Lin, A. Desmaison, L. Antiga, and A. Lerer, “Automatic differentiation in pytorch,” in *NIPS 2017 Workshop on Autodiff*, 2017.
- [50] H. Ohgaki and P. Kleihues, “The definition of primary and secondary glioblastoma,” *Clinical cancer research*, vol. 19, no. 4, pp. 764–772, 2013.
- [51] C. Lu, Y. Zhou, F. Bao, J. Chen, C. Li, and J. Zhu, “Dpm-solver: A fast ode solver for diffusion probabilistic model sampling in around 10 steps,” *Advances in Neural Information Processing Systems*, vol. 35, pp. 5775–5787, 2022.